Enhanced interface adhesion in shape memory alloy hybrid composites via an elastomeric interface: An experimental and numerical investigation

Gregorio Pisaneschi [a,*], Tommaso Maria Brugo [a,**], Paolo Cosseddu [a], Giulia Scalet [b], Andrea Zucchelli [a]

[a] Department of Industrial Engineering, University of Bologna, Viale Risorgimento 2, 40136, Bologna, Italy
[b] Department of Civil Engineering and Architecture, University of Pavia, Via Ferrata 3, 27100, Pavia, Italy

ABSTRACT

Shape Memory Alloy Hybrid Composites (SMAHCs) hold great promise for different applications. However, the interface between SMAs and the matrix presents challenges due to large strains associated with the martensitic transformations (MTs). Although different strategies have been proven effective in increasing interfacial strength, debonding and its prevention remain unresolved. Therefore, to enable MTs in SMAHCs, this paper proposes a novel solution using a rubber-like elastomeric interface. Pull-out SMAHC specimens were tested at different embedding lengths with and without the elastomeric interface. Specimens with the elastomeric interface showed better performance and stress-strain transfer during MT up to SMA wire breakage. The behaviour of the interface was studied using finite element analysis. A fine-tuning method was proposed for the cohesive zone model parameters. Simulated pull-out tests matched experimental data, revealing the debonding mechanisms. However, results with the elastomer underscored the need to fully represent the underlying physics of the highly deformable interface.

1. Introduction

Shape memory alloys (SMAs) are smart metallic alloys possessing the unique capabilities known as the super-elastic (SE) and shape-memory effect (SME). The SMA can recover its original shape through a diffusionless solid-state phase transformation, the martensitic transformation (MT), caused by the application of stress (i.e., SE) and/or temperature field (i.e., SME) [1,2]. Thanks to these unique capabilities, SMAs are employed in various applications [3]. Nevertheless, researchers are still exploring ways to expand their potential use. For instance, Ashby and Bréchet [4] proposed two ways: developing new alloys or creating hybrid materials. The latter can comprise fibre-reinforced polymers combined with SMA wires, creating SMA hybrid composites (SMAHCs) [5]. However, the few proven SMAHCs that have been developed did not directly incorporate SMAs into the morphing structure [6,7]. Integrating SMAs into composites can be challenging due to the large deformations associated with MT that can lead to debonding, which remains an open issue that must be addressed during both the curing and operation phases of SMAHCs [5].

Curing is pivotal in generating residual thermal stresses (RTSs) and transformational stresses from the shape recovery of pre-strained SMAs [8]. Mechanical frames can be used to address transformational stresses [9], but this can lead to the development of RTSs in the composite. Alternative solutions include cold-drawn wires to increase the reverse transformation temperatures [10] or low-temperature post-cures to prevent reverse transformation [11]. Another approach, first tried by Baz et al. [12] and then improved by Kluge et al. [13], uses sleeves, allowing the SMA to move freely within the composite. Nevertheless, the use of sleeves impacts composites, causing the reduction of their mechanical performances. If adhesion is required (e.g. when SMA is also used as a reinforcing element), the large strain due to MTs must be accounted for to prevent delamination. Various strategies have been proposed to enhance interfacial strength and address this challenge.

The surface modification strategy has been the primary approach adopted. Paine & Roger [14] embedded SMA wire using acid cleaning followed by hand-sanding and sandblasting as mechanical pre-treatments, showing better pull-out strength for the latter. These results were confirmed by Jonnalagadda et al. [15]. In both cases [14,

---

* Corresponding author.
** Corresponding author.
  E-mail addresses: gregorio.pisaneschi@unibo.it (G. Pisaneschi), tommasomaria.brugo@unibo.it (T.M. Brugo).

15], acid cleaning was ineffective; similarly, no improvements were obtained with acetone cleaning or deoxidation [16,17]. Besides chemical cleaning, other chemical treatments have been developed as the mechanical pre-treatments become unusable on small scales. Jang et al. [18] used different acids' etching on the wires and found that the pull-out force increased proportionally to the surface roughness increment. Smith et al. [19] added SMA surface chemical functionalisation with silane-coupling agents, improving the adhesion by roughly 100 %. Rossi et al. [20] found that treatment with basic solutions reduced adhesion. Some studies [21,22] used SMA ribbons instead of wire, which have larger areas for adhesion. Neuking and coworkers [21] investigated the impact of mechanical and electro-polishing, plasma treatment and coupling agents in different combinations, obtaining an improvement of 116 %. Hamming et al. [22] increased adhesion by surface-initiated polymerisation through a biomimetic initiator. High stresses were observed beyond MT, likely due to the interlocking effect of the matrix debris. As observed in other studies, the interlocking effect is one of the most effective strategies. For instance, Lau et al. [23] embedded twisted NiTi wires, and the geometrical changes increased the bonding strength, while Yuan et al. [24] indented the wires, and Choi et al. [25] used various modifications on the tips of embedded SMA fibres, and both increased several times the bonding strength. However, in all these cases, the predominant effect was geometrical anchoring, not adhesion. A less invasive approach is to deform the SMA prior to embedding (e.g. by SMA cold drawing [26] or axial pre-strain [27,28]) and then use the shape recovery to increase the contact pressure, thus enhancing the adhesion. Finally, another way to increase adhesion is to create a coating of the same matrix material [14,29]. The most relevant results are summarised in Table 1 and described below.

All the methods presented above have limitations. Mechanical and chemical treatment count on the roughness of the surface, potentially weakening the wire [14,15,18–21]. Geometrical modifications on the SMA wire alter its properties [23–26]. Even if some of these results reached high tensile stresses [22,25,28], the wire always detached from the matrix. The main cause could be the thinning of the wire at the debonding front [30], as first hinted at by Paine et al. [14], who also suggested that a ductile coating could accommodate the induced strains.

1.1. Research significance

The objective of this research was to create a functional morphing structure. Povolo et al.'s prior research results [31] inspired the approach to mitigating debonding between composite and metal using a rubber-like elastomeric interface. A feasibility study presented at the ICCM conference by the authors [32] demonstrated the potential of using an elastomeric material as an interface for embedding SMA wires

in glass fibre-reinforced plastic (GFRP). Two types of interfaces, elastomeric and not, were compared using pull-out tests. Material characterisation and manufacturing were limited to demonstrate the potential for a single embedding length. The numerical analysis only considered the 2D cohesive zone model (CZM) without validation and with limited and approximated material models. Moreover, RTS analysis was not included.

The present investigation comprehensively and systematically addresses the study inherent in the engineering process of SMAHC using elastomeric interface materials. Different SMAHC specimen lengths were manufactured and compared using pull-out tests. The process proved simple and effective and ensured excellent stress distribution, which allowed MTs of the embedded SMA wire until its breakage. In addition, 2D and 3D finite element analysis (FEA) was performed to study RTS and the pull-out process. An improved hybrid numerical-experimental method was developed to fine-tune the cohesive zone modelling parameters. The FEA revealed the debonding mechanism for different lengths but showed limitations in comprehensively representing the physics of the elastomeric interface, which remains out of the scope of this study.

2. Experimental investigation

Two methods of embedding SMA wires in GFRP composite laminates were investigated - one with direct contact with the epoxy matrix and the other with an elastomeric interface. The interfacial adhesion strength was estimated by pull-out tests. Different approaches can be used to evaluate a single fibre interfacial shear strength (IFSS, τ_i). If the shear stress distribution along the embedding length is considered constant [33], the IFSS can be calculated as:

$$\tau_i = F/(\pi \cdot D_f \cdot L_e), \tag{1}$$

where F is the pull-out force, D_f is the diameter of the wire, and L_e is the embedded length. This approximation underestimates the value as L_e increases because the shear stress distribution is not constant and reaches max values near the free edges [34]. Other methods were developed; for instance, Payandeh et al. [35] developed an analytical calculation to determine the IFSS in long SMA wires embedded in bulky epoxy. Still, closed-form solutions require knowledge of the material's elastic properties, which are considered linear and homogeneous. However, in the present study, the SMA wires are embedded in a non-homogeneous, orthotropic material (GFRP) that can be interfaced with a non-linear elastomeric material. Therefore, it was preferred to evaluate the maximum IFSS experimentally by decreasing L_e until an asymptotic behaviour is reached; the IFSS can be assumed uniformly

Table 1

Comparison of adhesion strengthening methods by means of pull-out results. [*]: results obtained in the present study. In column "SMA" is specified what type of material was used as embedded fibre; in column "Matrix" is specified the embedding medium; in column "Treatment/notes" is specified the treatment for adhesion used or a state of the wire; in column "Wire MT" is specified if the martensitic transformation happened in the free/embedded wire and in what phases (A: austenite, M: martensite, M+: detwinned M, SIM: stress-induced M); in column "σ_{max}" is specified the wire axial stress. The IFSS is calculated with Eq. (1). Other results are reported in supplementary Section 2.

Ref.	SMA	Matrix	Treatment/notes	Wire MT	σ_{max}	IFSS	L_e	L_e/D_f
–	–	–	–	–	(MPa)	(MPa)	(mm)	–
[23]	SME	Epoxy	Twisted	M − M+ free	735	7.7	12	24
[28]	SME	Epoxy	6 % pre-strain	M − M+ free	604	1.7	30	88
[28]	SME	Epoxy	6 % pre-strain, heated	A - SIM free	1057	3.0	30	88
[20]	SME	Bi-component	Acid/basic/acid etching	No	190	7.6	5	6
[20]	SE	Bi-component	Acid/basic/acid etching	No	380	15.2	5	6
[21]	SE	PA6	Polishing, plasma coupling agent	A - SIM free	650	8.6	20	12
[22]	SE	PMMA	Surface initiated polymeriz.	A - SIM free	1026	2.2	15	118
[26]	SME	Mortar	cold drawing	M − M+ emb.	154	2.6	15	15
[25]	SE	Mortar	Spear-head	A - SIM emb.	799	10.0	15	15
[29]	SME	ABS	Laser-gas-nitration	M − M+ emb.	660	1.3	10	125
[*]	SE	GFRP	–	No	214	13.5	0.8	4
[*]	SE	GFRP	Elastomeric coating	A - Break	1165	0.8	76.2	381

distributed [20], and Eq. (1) was thus applied.

Moreover, austenite has a higher pull-out load than martensite [36]. Thus, SE wires were used to avoid excessively small embedding lengths to reach the peak value of the IFSS without reaching the MT. Materials, fabrication, testing, and experimental results are presented and discussed in the following section. All the tests were performed with an electro-mechanical universal testing machine (Instron series 5966) equipped with a 10 kN load cell.

2.1. Materials and methods

The wires were embedded in a GFRP E-glass 8H Satin 300 g/m^2 epoxy matrix prepreg (VV300S - DT120H-34 supplied by Delta-Preg) with a cured thickness of 0.22 mm and a glass transition temperature (T_g) of 120 °C.

The elastomeric interface used in this study is a cross-linking elastomeric layer (KRAIBON® AA6CFZ, supplied by KRAIBURG GmbH) with a thickness of 0.5 mm. It is a product designed to be co-cured with thermosetting resin to bond metals and composites. It offers a permanent bond comparable to that of structural adhesives, and, in addition, it can thermally and electrically decouple materials, making it particularly suitable for the integration in composites of SMA operated with electricity. Tensile and compression tests, according to ISO 527-3 and the ISO 7743 standard, respectively, were performed to obtain the elastic properties of the elastomer (Fig. 2 a and b). Additional data are reported in supplementary Section 1.

The SE wire is a high-strength Ni–Ti wire from SAES® with a nominal composition by weight of 55.8 ± 0.5 % nickel, titanium balanced, O, Fe, and C, all under 0.05 %. It has a diameter of 0.2 mm and a light oxide surface (amber). The austenite start and finish temperature are equal to −25 ± 12 °C and −8 ± 16 °C, respectively, as reported by the manufacturer. The SMA wire tensile behaviour was characterised under displacement control at 4 mm/min speed, with a free length of 50 mm and at room temperature, according to ASTM F2516-18. The effect of the crimping system was investigated by either crimping the wire's ends or pressing them between two brass plates. In addition, the curing temperature, which can alter the wire properties [37], was also examined by testing the wire in its original state and after undergoing the curing cycle used for the SMAHC.

2.1.1. Manufacturing of specimens

As discussed by Pattar and Patil [38], the fabrication process presents many challenges, such as the positioning of SMA in the composite. Therefore, the specimens were produced by stacking GFRP prepreg and KRAIBON® plies in a 3D-printed fixture (iglidur® i180 filament), as shown in Fig. 1, which allowed to align the wire and control the crucial embedding length precisely. A Teflon sheet, 0.5 mm thick, was placed over the plies and fixture to level the material during curing and prevent sticking to the release film. SMAHC specimens were manufactured with two types of stacking sequences, one with the epoxy interface (here abbreviated as specimen EP) and one with the elastomeric KRAIBON® interface (here abbreviated as specimen KR):

EP) [GFRP-0$_3^\circ$/SMA/GFRP-0$_3^\circ$]

KR) [GFRP-0$_1^\circ$/KRAIBON$_1$/SMA/KRAIBON$_1$/GFRP-0$_1^\circ$]

Both laminate types were cured in an autoclave with an isothermal of 120 min at 120 °C to ensure the complete epoxy and rubber-like interlayer cross-link. The heating and cooling ramp was 2 °C/min, and 3 bar pressure and 0.95 bar vacuum were applied to the entire cycle. Specimens with multiple embedding lengths were fabricated, ranging from 1/32 to 3 inches (0.8 mm–76.2 mm) for the EP and 1/16 to 3 inches (1.6 mm–76.2 mm) for the KR. Four pull-out test specimens of 20 mm in width were produced for each embedding length.

2.1.2. Pull-out test setup

How samples are clamped in pull-out tests can significantly impact the results. The fixed bottom loading method (FBC) and restrained top loading method (RTC) are often used as standard approaches [39,40]. However, given that the wire was embedded in a laminate plate instead of a bulky epoxy, a non-standard test was chosen [9]. The specimen was clamped at the sides using a customised fixture to prevent sideways movement (the clamping area is indicated by the red squares in Fig. 2 c). A 10-mm-wide window was left between the clamping to ensure that the interfacial stresses on the wire were not affected by the stress generated by the pressing plates. On the other side, a mechanical wedge grip held the wire between two brass plates. The free wire length was 25 mm. Tests were conducted under displacement control at 2 mm/min constant speed, i.e. at the same strain rate as the SE wire tensile test, to avoid incongruity due to strain-rate dependence of SMA [41].

2.2. Results and discussion

The results of the SMA wire tensile tests (reported in supplementary Section 1) confirmed that the wire's properties remained consistent before and after curing, and the best configuration was the one with brass plates. Nonetheless, Pagliaro and Panciroli's findings show that using a ductile tab allows for wire testing, avoiding slippage and preventing stress concentration [42]. In Fig. 3, the black dotted curve represents the tensile test result for the brass plate clamped wire. FEA results of material models are added and will be further discussed in the numerical section.

2.2.1. Manufacturing

The SEM micrography in Fig. 4 a) shows the cross-section of the SMA wires embedded in the two types of specimens after curing. In the EP specimen, the glass fibres surround the wire and create an "eye", resulting in a resin pocket, also observed in the work of Otsuka and Ren
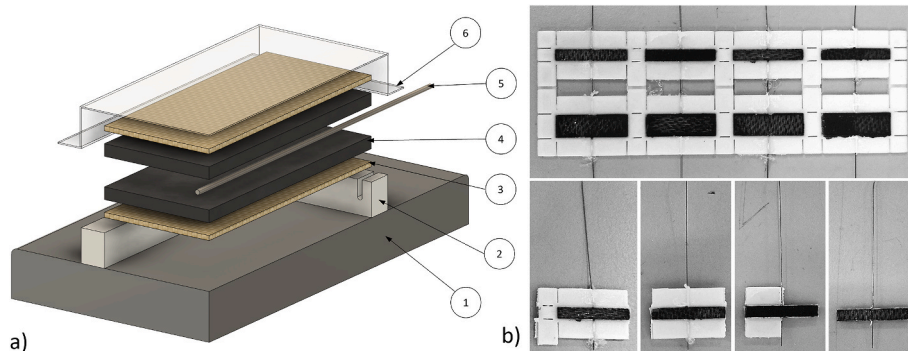

Fig. 1. Specimens manufacturing of KR (EP is similar and not represented here). a) Lamination setup: (1) steel plate, (2) 3D printed mask, (3) GFRP, (4) KRAIBON®, (5) SMA, (6) PTFE sheet. b) Separation of samples thanks to mask pre-cuts.
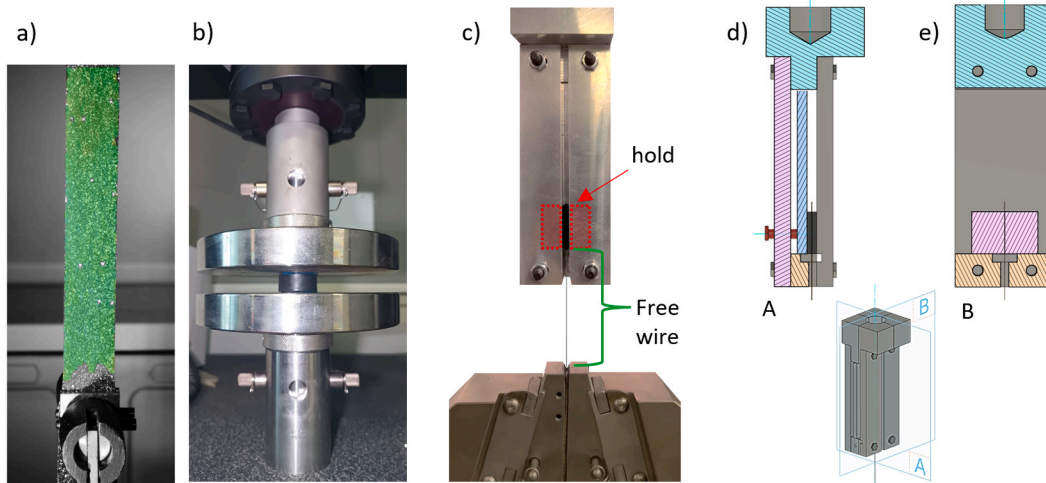
Fig. 2. Testing setups. KRAIBON® tests: a) tensile with DIC, b) compression. Pull-out tests: c) setup, d) middle cross-section along plane A, e) middle cross-section along plane B.
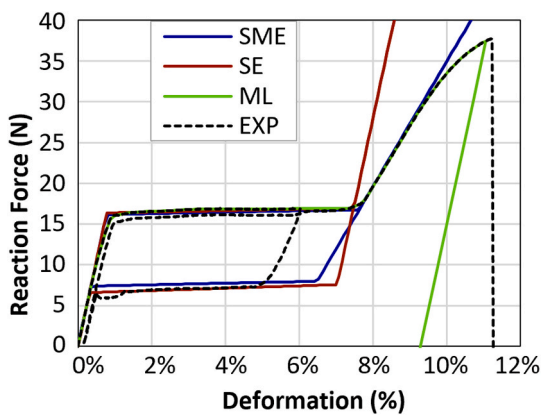

Fig. 3. Tensile test result and finite element models (FEMs) response of the SE wire.

[43]. The KR specimen cross-section shows the SMA wire embedded in between the elastomeric layers and the GFRP plies that sandwich them.

2.2.2. Pull-out tests

In Fig. 5, the overall pull-out behaviour is described by the respective curves of the EP (yellow curve) and KR (blue curve) specimens with a 1" embedding length. The tensile response of the not embedded SMA wire, with a free length of 25 mm (dotted black curve), is overlapped as a reference. In specimen EP, the MT of the free wire begins (represented by the orange symbol Δ) at approximately 17 N, reaches a plateau of 18 N (i.e. 570 MPa normal stress in the wire) and continues until completion (**o**). Up to this point, the EP exhibits a behaviour that overlaps with the free wire due to the high stiffness of the epoxy interface. Once the free wire has completely transformed, the MT continues within the embedded wire. The debonding process starts (**x**) following the MT propagation until the wire completely detaches (**+**). In Fig. 5, the small images below the EP curve show the progression, thanks to the GFRP transparency. In addition, a slight force increment can be observed during debonding that could be attributed to debris interlocking.

In specimen KR, the MT of the free wire starts (represented by the violet symbol Δ) at around the same force as the EP but at a more significant displacement due to the more compliant embedding medium.
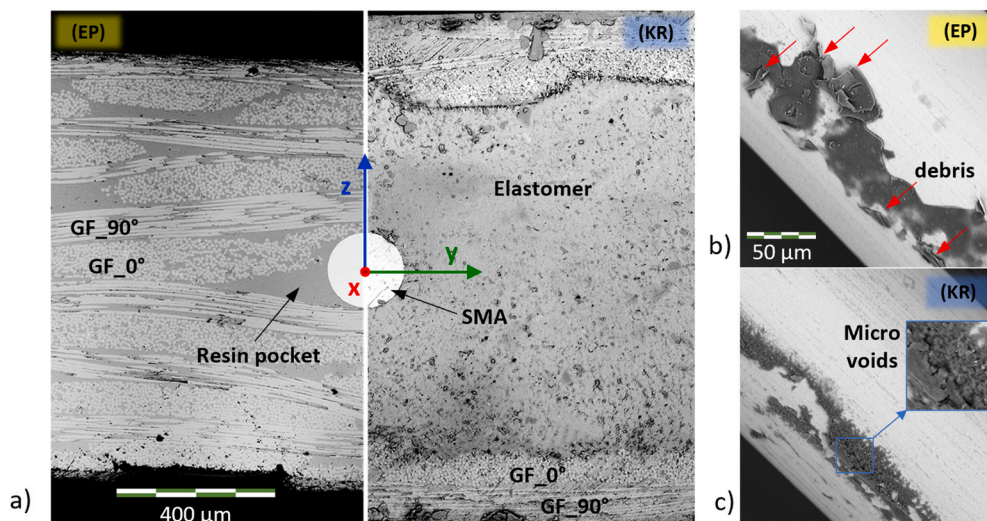

Fig. 4. SEM micrography. a) Section of EP (left) and KR (right) specimens after curing. b) EP and c) KR pulled-out wire.
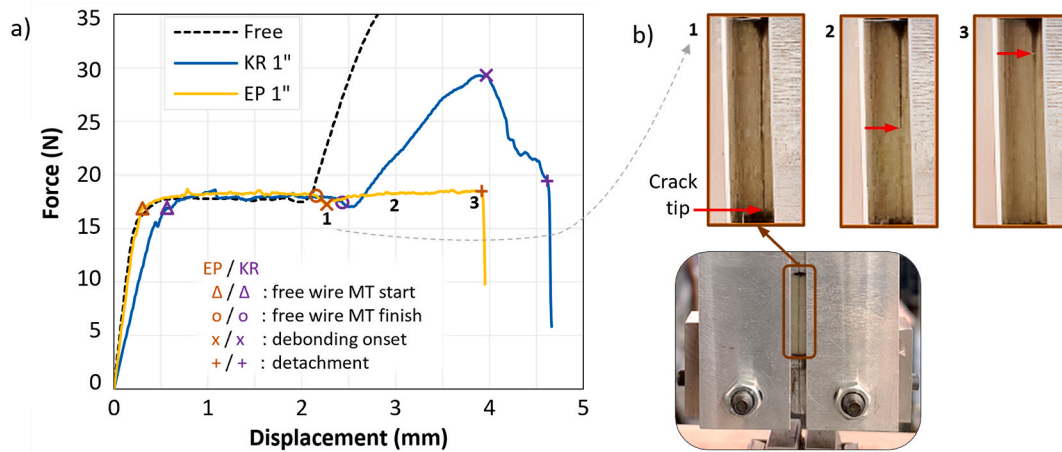
Fig. 5. Force-displacement for 1″ EP (yellow line) and KR (blue line) specimens pull-out and the equivalent tensile behaviour of the free SMA wire (dotted black line); b) advancement of the crack tip in the EP specimen.

When the free wire is completely transformed (**o**), the force rises again. The force increment slope is lower than that of the free SMA wire, indicating a further deformation of the elastomer, and presumably, the MT starts in the embedded wire. Contrary to what happens in specimen EP, in KR, thanks to the elastomeric interface, which adjusts to the large deformation of the wire, the force increases until debonding onset (**x**) at around 30 N (equivalent to 950 MPa in the wire). After the debonding onset, a rapid delamination develops until the wire completely detaches (**+**).

Additionally, Fig. 4 b) and c) show the wire surface after being pulled with some debris, indicating good adhesion. In the fracture surface, the debris of the EP appears smooth, suggesting a fragile behaviour. In contrast, the debris in the KR appears jagged with some micro void coalescence, suggesting a ductile behaviour of the interlayer [44].

In Fig. 6, the reaction force versus the displacement recorded by the test machine is reported for different EP and KR embedding lengths (L_e). All results obtained from the force-displacement curves are reported in supplementary Section 2. For clarity, Fig. 6 reports only results that showed different responses (e.g., the EP with L_e 1/8″, 1/4″, 1/2″, 1″, and 3″ overlapped, having a shorter or longer debonding). All specimens tested failed by complete debonding except for 3″ KR specimens in which the wire broke due to reaching the ultimate strength of the SMA.

The stiffness of the first slope of both EP and KR specimens increases with L_e, as shown in Fig. 6. Specifically, the EP specimens reach maximum stiffness at 1/8″ length. In contrast, the KR ones reach it at 1″, exhibiting a more compliant interface. This length at which the stiffness ceases to increase is termed the *critical embedment length for maximum*

stiffness ($L_{e,k}$). So, in the case of EP $L_{e,k} = 1/8″$ and for KR $L_{e,k} = 1″$.

The force-displacement curve of the 1/16″ KR specimen shows a pronounced bilinear behaviour, which is consistent with the stress-strain curve of the elastomer (reported in supplementary Section 1), characterised by a knee. Such a behaviour can be attributed to a uniform tangential stress distribution. In contrast, for embedding lengths greater than 1/16″, the not uniform shear stress distribution, with a localised knee, masks the bilinear behaviour of the material. Other two critical embedding lengths, described by Dawood [45], can be identified: one ($L_{e,S}$) when MT starts in the free wire, and the force stops increasing, exhibiting a plateau; the second one ($L_{e,F}$) when the MT in the free wire finishes. These lengths are coincident ($L_{e,S}=L_{e,F}$) both for EP and KR and equal to 1/16″ and 1/4″ respectively, the latter being greater. Therefore, the EP embedding solution seems more promising at these lengths. Beyond $L_{e,F}$, the MT develops in the embedded wire: in the case of EP specimens, the advancement of the MT is followed by debonding onset and propagation, and the maximum force does not increase; on the contrary, in the case of KR specimens, the force increases, demonstrating that despite the MT, the embedded wire is still adhering.

In the bar graph of Fig. 7, the IFSSs, calculated according to Eq. (1), are reported for each embedding length and interface type. It is shown that by reducing the embedding length, the IFSS increases. However, below a value, here called *constant stress critical embedment length* ($L_{e,c}$), the IFSS reaches an asymptote. This can be attributed to the fact that, as the embedding length decreases, the shear stress gradient at the free edge reduces to a uniform distribution. It can be safely assumed that in EP specimens, $L_{e,c}$ is between 1/16″ and 1/32″, while in KR, it is between
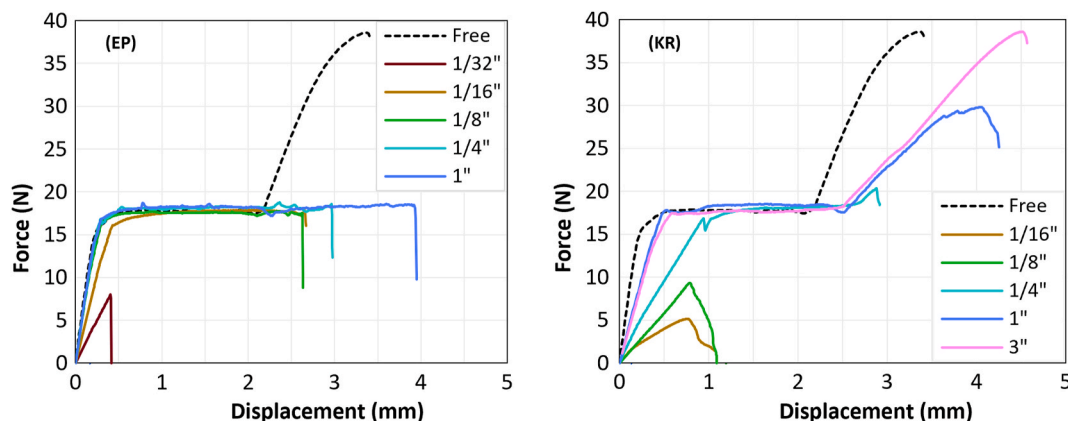

Fig. 6. Pull-out force-displacement curves for specimens with different lengths, of EP on the left and KR on the right.
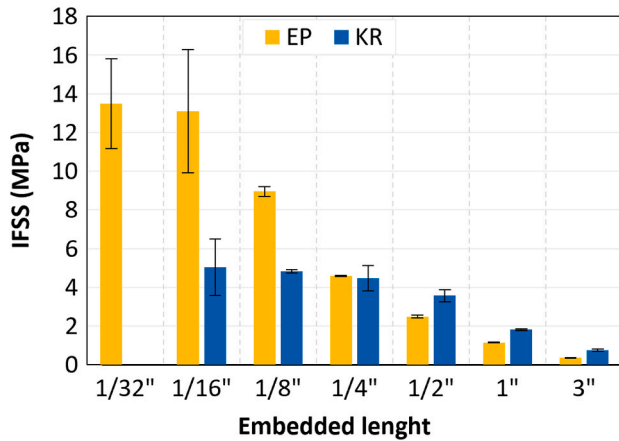
Fig. 7. Calculated IFSS reported for EP and KR specimens for all the embedded lengths.

$1/16''$ and $1/8''$. For this length, the calculated IFSS can be considered identical to the maximum shear stress ($\tau_{i,max}$) and equal to 13.5 MPa and 4.8 MPa for EP and KR, respectively. It can be observed that EP has higher IFSS for smaller specimens, while KR shows higher values for lengths above $1/4''$ thanks to the more compliant interface.

Finally, wire breakage occurs in KR specimens larger than $1''$ before debonding. To the author's knowledge, this is the first time that it was observed that the embedding interface strength is higher than the SMA wire tensile one. Table 1 summarises the most interesting results reported in the literature. Despite the improved adhesion, the embedded wire undergoes MT only in a few cases, and in no cases does it break. This can be explained by considering a fourth length, the *ultimate critical length* $L_{e,u}$, at which the wire breaks. If it is considered only a shear stress, uniformly distributed, it can be assumed that $L_{e,u} = \sigma_{f,R} * D_f / \tau_{i,max}$ ($\sigma_{f,R}$ is the ultimate stress of the wire and D_f its diameter [33]). Delamination occurs when $L_e > L_{e,u}$ in EP samples and all cases in the literature, supposedly due to the radial stress caused by the thinning of the SMA wire. On the other hand, in KR samples, the wire breaks when $L_e > L_{e,u}$. This is likely due to greater compliance, which allows for better redistribution of stresses and neutralisation of radial stresses rather than an increase in IFSS. Finally, observing the L_e/D_f ratio in Table 1 [33], it is evident that a lower ratio results in a higher IFSS (i.e. small L_e values are recommended to measure $\tau_{i,max}$ [46]).

3. Numerical investigation

In this study, FEAs were conducted using the commercial software ANSYS® Mechanical Workbench 2023. The simulations aimed to model the distribution of residual thermal stress (RTS) after curing and stress distribution during pull-out and debonding processes. In these preliminary simulations, ANSYS® shared topology option was used, sharing the node between the wire and the matrix at the interfaces, with a conforming mesh, assuming perfect adhesion. A 3D finite element model (FEM) was created to represent the geometry and the boundaries accurately. However, adding elastomer hyper-elastic behaviour with deformation beyond 100% drastically increased the computational time and made convergence challenging. Therefore, a simplified axisymmetric 2D model was validated against a 3D model and the experimental results. Finally, the cohesive zone model (CZM) formulation was implemented in the axisymmetric 2D model for the SMA-matrix interface. After defining first-attempt values for the CZM parameters, fine-tuning was performed by design of experiments (DOEs) on a $1''$ embedding length for both EP and KR. Validation on different lengths followed. All data reported here are results of the 2D axisymmetric model simulations; further information on 3D and shared nodes simulations is reported in supplementary Section 3.

3.1. Finite element models

All the non-linear simulations were performed under displacement control and solved with the implicit Newton-Raphson method and direct solver. Automatic time stepping was adopted. Only simulations with hyperelastic models had large deflection turned on. Such an option did not improve the accuracy for all other simulations but impacted the computational time and was thus turned off. During wire detachment rigid motion, a non-linear damping coefficient was set with a constant energy dissipation ratio of 10^{-4} to stabilise the simulations.

3.1.1. Mesh and boundary conditions

Fig. 8 shows the geometry and boundary conditions of the 2D FEM, which represent a cylindric volume inside the specimen with a radius equal to the thickness. The geometry was discretised with a conforming mesh and linear elements PLANE 182, which provided a good balance between capturing the essential features of crack growth and maintaining computational efficiency. The FEM used in CZM simulations was the same as in the one with shared nodes, except for the CZM linear interfacial elements (INTER 202) interspersed between the SMA wire and the matrix. In the case of KR specimens, the interfacial elements also substituted the elastomer. After convergence tests, the mesh was refined in the radial direction at the interface with an element dimension of 0.001 mm; along the axial direction, it was kept around 0.001 mm to simulate correctly the CZM debonding for the whole embedding length.

The boundaries of the FEM with shared nodes and CZM varied depending on whether the thermal effects were considered or not. If they were considered, a two-step simulation was used. In the first step, simulating cooling after complete cross-linking (120–25 °C), a remote point at the side of the specimen allowed free movement. In the second step (pull-out), by means of an ANSYS® APDL script, the remote point displacement was constrained in the pulling direction, starting from the position reached at the end of the first step. If thermal effects were negligible, a one-step pull-out simulation was set, and the displacement in the nodes at the side of the specimen was constrained in the pull-out direction. A linear path *P1–P2* along the interface was used to observe the results of the simulations.

3.1.2. Material models

GFRP was modelled as an orthotropic material. Elastic and thermal cartesian properties were taken from the Hexcel© E-glass fabric datasheet [47]. In Table 2, the equivalent elastic and thermal properties in the cylindrical coordinate system used for the 2D model are reported. Note that the same thermal and elastic properties were considered in the radial and circumferential directions and equal to the GFRP ply out-of-plane properties. This simplification can be considered reasonable if looking at the micrograph of the EP specimen cross section (Fig. 4
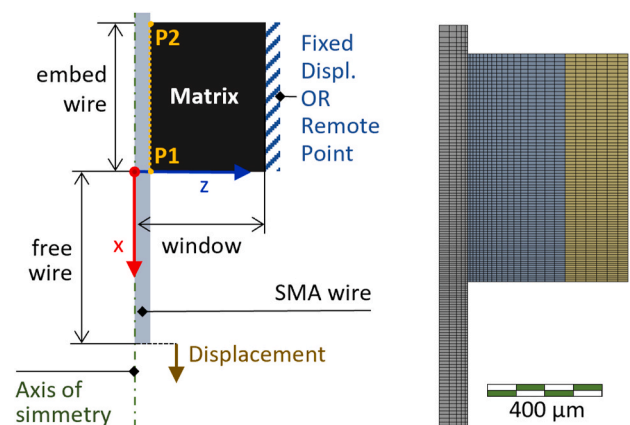

Fig. 8. On the left, the FEM with boundaries and path P1–P2 (orange dotted lines); on the right mesh of the $1/32''$ EP specimen.

Table 2
Properties of GFRP.

Elastic modulus (MPa)			Poisson's ratio			Shear modulus (MPa)			CTE (°C^{-1})		
E_Z	E_θ	E_r	$\nu_{Z\theta}$	$\nu_{\theta r}$	ν_{Zr}	$G_{Z\theta}$	$G_{\theta r}$	G_{Zr}	CTE_Z	CTE_θ	CTE_r
20000	9000	9000	0.28	0.4	0.28	4000	3800	4000	14 E−6	25 E−6	25 E−6

a), in which the presence of the resin pocket around the wire reduces the transversal stiffness.

A 5th-degree Mooney Rivlin model was chosen for KRAIBON® after testing different hyperelastic material models based on uniaxial tests data curve fitting. Material constants (C10–C02) are reported in Table 3. D1, the incompressibility parameter, was calculated as $D1=2/K$, where K is the Bulk Modulus derived from the relation $E=3K(1–2\nu)$ where E is the Young's modulus and ν the Poisson ratio, reported in the supplementary Section 1.

For the SMA wire, different models were compared to find the optimum between a correct representation of the pull-out and computational cost. Two SMA material models are available on ANSYS simulating the SE (based on [48]) and the SME (based on [49]). The properties and parameters identified from the experimental curve of Fig. 3 are listed in Table 4 (as described by Refs. [2,50,51]). In addition, the multilinear hardening plasticity model (ML) was tested (e.g. Antico and Zavattieri [30] used a hardening model for the NiTi wire's response under monotonically increasing stress). Fig. 3 shows that the SE model approximates the second linear slope with the slope of the austenite Young's modulus, which is usually higher than the martensite one. In contrast, the SME model can correctly represent it. However, the latter is computationally more expensive and less stable when converging with CZM. Instead, the ML model is the optimum between simulation time and correct representation of the phenomenon, except for the delaminated wire, which recovers the stress with a linear stiffness and a permanent deformation instead of the non-linear reversible SMA springback behaviour.

3.2. Shared nodes interface FEAs results and discussion

RTSs occur during cooling after curing due to the difference between the coefficients of thermal expansion (CTE) of the SMA and the polymeric matrix [30]. The residual stress-free temperature, at which the stress is null [52], was assumed to be the same as the curing temperature because it coincides with the T_g (120 °C). It is worth noting that the shrinkage of epoxy resins below T_g decreases linearly with the drop in temperature [53]. RTSs were analysed by means of shared node simulations for different lengths. The results are reported in Fig. 9 a) and b) for 1/4″ EP and KR specimens, respectively (higher lengths did not produce increments of the RTSs). Regarding EP, the normal (radial) stress exhibits an average of −8.7 MPa (compression) and a traction peak of 3.9 MPa at the free edge. The tangential (shear) stress reaches 4.3 MPa peaks, while the average is zero. These values held significant weight and were considered in all CZM EP simulations.

In KR specimens, the normal stress average is −0.5 MPa, with a traction peak of 2 MPa at the free edges. The tangential stress reaches a peak value of −0.9 MPa, while the average is zero. These values were considered negligible and, therefore, were not considered in the CZM FEAs.

After the thermal analysis, the pull-out test was performed, applying the maximum experimental force. By means of the simulation, it was

observed that the MT starts from the side of the wedge gripper in the free wire, and once it reaches the embedded side, the stress arises at the interface near the free edge. In the plots in Fig. 9 c) and d), the stress developed along the path P1–P2 at the maximum pull-out force is shown. In the case of the EP, normal and tangential stress peaks are comparable (as also seen in Refs. [30,54]) and rise to 35 MPa and 60 MPa, respectively. The shared nodes simulations result in high EP peak stresses at the embedding ends, which is reasonable with the hypothesis of a perfect bond [55]. On the contrary, KR stresses are around one-tenth of EP ones, and normal stress is about one-fifth of the tangential stress. Further information is reported in the supplementary Section 3.

3.3. CZM parameters

In the CZM model, the interface between the SMA and the matrix was represented by a mixed-mode bi-linear cohesive damage law model [56]. This model is based on traction-separation laws in which the variables are the normal and tangential traction (t_n, t_t), the relative displacement jumps (δ_n, δ_t), and the relative stiffness (K_n, K_t). In Fig. 10, the bilinear law for normal and tangential traction is shown by the black lines. δ^* and δ_C are, respectively, the displacement jump at maximum traction (t_{max}) and at debonding completion, K is the stiffness and G the energy. A combined energy criterion is used to define debonding completion by the non-dimensional effective displacement jump λ, for mixed-mode fracture, according to the following equation:

$$\lambda = \sqrt{\left(\frac{\delta_n}{\delta_n^C}\right)^2 + \beta^2\left(\frac{\delta_t}{\delta_t^C}\right)^2}. \tag{2}$$

When λ is larger than $\lambda_{cr}= \delta^*/\delta_C$, the damage parameter affects the behaviour at the interface, with degradation of the stiffness while the bonding energy gradually decreases until the cohesive element is completely detached [57]. Therefore, the model inputs for Mode I and II are the maximum stresses, the variable α (equal to λ_{cr}) and δ_C. From these values, energy for Mode I and Mode II, GI and GII, are calculated as the area of the triangle in Fig. 10.

3.3.1. Evaluation of parameters for mode I and mode II

Compared to the previous study [32], the fine-tuning method was improved to reduce the DOE in one step, starting from choosing first-attempt values for CZM parameters, summarised in Table 5. For Mode II, the first-attempt parameters were derived from the experimental curves (Fig. 6) of the 1/32″ and 1/8″ specimens for EP and KR, respectively, the longest lengths for which MT did not occur, and in the case of KR also the length not presenting the knee due to the bilinear behaviour of the elastomer. The experimental force-displacement curve was adjusted by subtracting the compliance of the free wire to determine the accurate tensile separation law. From this, the maximum traction separation ($t_{t,max}$), δ_t^*, and $\delta_{t,C}$ were extrapolated. The stiffness K_t was then calculated as $t_{t,max}/\delta_t^*$. The α value, equal for both Mode I and II, was calculated as $\delta_{t,C}/\delta_t^*$. For Mode I, the first attempt value of the normal maximum stress ($t_{n,max}$) was estimated from the 1/4″ simulation with shared nodes, the minimum L_e at which the MT occurs in the embedded wire for both EP and KR. An average traction value along the path P1–P2 was calculated for EP and KR. To estimate the remanent parameter, k_n, the interface's normal and tangential stiffness ratio was assumed to be the same ratio as the young and tangential modulus (E/G) from the theory of elasticity. For EP, E/G was calculated using datasheet values, while for KR, it was calculated as $2*(1+\nu)$ using the

Table 3
5th-degree Money Rivlin model parameters for the KRAIBON®.

C10 (MPa)	C01 (MPa)	C20 (MPa)	C11 (MPa)	C02 (MPa)	D1 (MPa^{-1})
−2.260 E−1	1.302 E+0	7.785 E−2	−1.212 E−1	4.567 E−2	1.120 E−1

Table 4

SMA wire properties from engineering data of the tensile test.

Austenite modulus (MPa)	Hardening parameter (MPa)	Austenite finish temp. (°K)	Elastic limit (MPa)	Temp. scaling parameter (MPa/°K)	Transform. max strain (%)	Martensite modulus (MPa)	Load Dependency Parameter
E_A	h (C1)	A_S (C2)	R (C3)	β (C4)	ε_L (C5)	E_M (C6)	(C7)
67540	168	248	107	6.40	7.27	25400	0
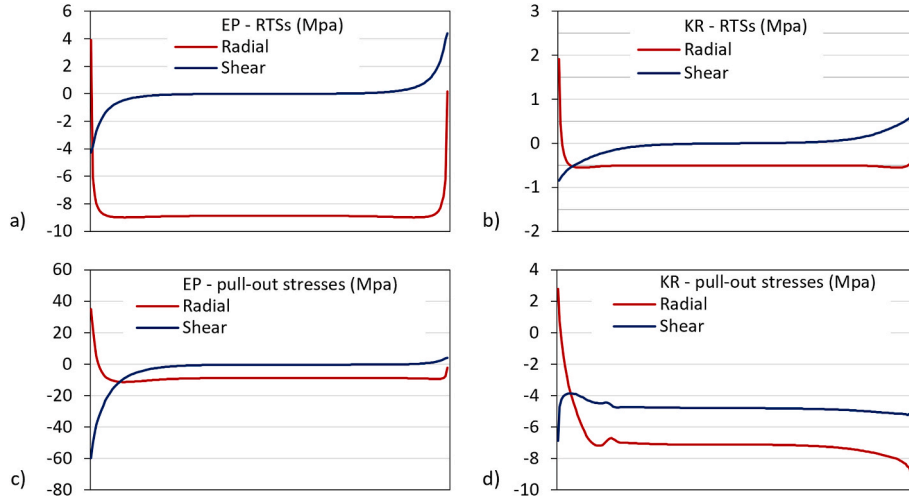
Fig. 9. Normal (radial) and tangential (shear) stresses on the interface along the path *P1–P2* for the 1/4″ simulations of EP (left) and KR (right). Above are the results of the first thermal step (RTS), and below are the results of the second pull-out step.
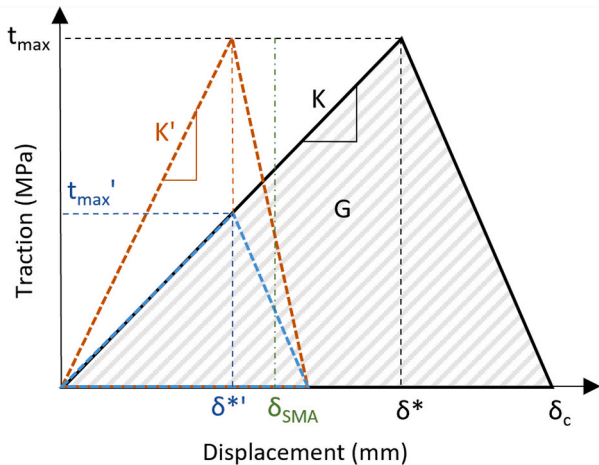

Fig. 10. Bilinear CZM law representation (black lines); in blue and orange dotted lines bilinear laws examples with δ*<δ_SMA.

experimental value of the Poisson coefficient from the tensile tests (ν = 0.42). Starting from these parameters, it was possible to calculate δ_n^*, and $\delta_{n,C}$.

3.3.2. Fine-tuning of the CZM parameters

Based on preliminary DOE results reported in supplementary Section

4, some assumptions were made to define the presented method. The results obtained for EP preliminary DOE allowed to assume the following.

1. Increasing *GI* or *GII* influences the debonding starting force.
2. The maximum displacement slightly increases by increasing $t_{t,max}$, while it negligibly changes by increasing $t_{n,max}$.
3. The variation of α changes the results negligibly; for a value close to 1, convergence issues arise.

From points 2 and 3, it can be assumed that the stiffness of the CZM has negligible influence on the results of EP specimen. In addition, it was found that the influence of the coefficient friction (to consider the interference due to RTSs when the wire detaches) is negligible.

For KR specimen, the results obtained from the preliminary DOEs allowed to assume the following.

1. Variation of K_t greatly influences the overall stiffness and the debonding force, while variation of K_n does not.
2. Increasing *GII* increases the debonding force, while increasing GI does not influence it.

Contrary to what was observed for the EP specimen, in the case of the KR interface, the *Mode I* parameters do not influence the results. That is because $\delta_n^* >> \delta_{SMA}$ (qualitatively represented in Fig. 10), where δ_{SMA} is the maximum radial displacement that the wire can achieve (around 0.01 mm). It is worth noting that if the interface is very stiff (e.g. orange

Table 5

First-attempt parameters for EP and KR DOEs.

	$t_{n,max}$	δ_n^*	$\delta_{n,C}$	K_n	GI	$t_{t,max}$	δ_t^*	$\delta_{t,C}$	K_t	GII	α
	(MPa)	(mm)	(mm)	(MPa/mm)	(MPa*mm)	(MPa)	(mm)	(mm)	(MPa/mm)	(MPa*mm)	–
EP	2.7	0.0033	0.0035	814	0.0047	13.5	0.040	0.042	380	0.28	0.96
KR	2.8	0.15	0.21	19.2	0.29	4.83	0.72	1.03	6.76	2.48	0.70

dotted curve with K' in Fig. 10), it is necessary to have a high $t_{n,max}$ to avoid delamination due to *Mode I*, while if the maximum normal traction is low (e.g. blue dotted curve with t_{max}' in Fig. 10), the alternative is to reduce K_n. Having $\delta_n^* >> \delta_{SMA}$ also implies that the normal traction can be influenced only by the KRAIBON® deformation, which is partially represented in the CZM simulations where the interfacial elements substituted the thick layer of elastomer, missing tangential-normal stresses coupling [58]. Nevertheless, the normal stress determined by the pull-out simulation with shared nodes was only a third of the tangential stress. Consequently, the CZM approximation, albeit less precise, can provide a representative depiction of the macro behaviour during pull-out and allows for the observation of Mode II behaviour.

The present DOEs run on $1''$ specimens, as this is the length at which both EP and KR specimens covered all the wire transformation phases. Starting from first-attempt values (Table 5), a DOE with *GI* values varied between 1/16 and 16 times was run, keeping the stiffness constant. A script in APDL allowed to extrapolate results versus time: normal stress, tangential stress, displacements, and reaction force. These outputs were crucial in assessing the accuracy of the fitting between FEM and experimental results. Additionally, the APDL script captures the results of CZM interface elements (stresses and displacements for each substep), which are absent in Mechanical. The APDL scripts are reported in the supplementary Section 5. The DOEs yielded the following outputs: maximum reaction force (MRF), displacement at delamination start (DDS), which was considered when tangential stress in the first interfacial element drops below 0.1 MPa, and displacement at delamination finish (DDF) considered when the reaction force drops below 1 N. The output results of each simulation were tested against average experimental values.

i. (MRF$_{exp}$ - DEV) < MRF < (MRF$_{exp}$ + DEV)
ii. (DDS$_{exp}$ - DEV) < DDS < (DDS$_{exp}$ + DEV)
iii. (DDF$_{exp}$ - DEV) < DDF < (DDF$_{exp}$ + DEV)

where DEV was considered equal to the experimental standard deviation. Those that better fit the MRFexp and delamination length (DDF-DDS) were chosen between the values satisfying these conditions.

3.4. Results and discussion

The DOE optimal CZM parameters obtained for KR and EP are reported in Table 6.

In Fig. 11, the force-displacement curves resulting from the simulation for different SMA material models are compared with experimental ones for different embedding lengths. It can be observed that for the EP, the optimal parameter allows for an accurate description of the adhesive behaviour of the epoxy-SMA interface at all lengths. During the simulation, the delamination progression always follows the MT while the reaction force remains constant. In all the EP lengths, the initial moment of delamination coincides between FEAs and experiments. Regarding the different SMA material models, it can be observed that both SE and SME (this simulated only for $1''$) exhibit similar results to the ML model. The computational time required for ML and SE models was comparable. In contrast, the SME simulations needed a mesh refinement, only converging until detachment and requiring ten times the computational time. The KR DOE has resulted in a sub-optimal parameter combination, which gives accurate results only for small lengths (second row in Fig. 11). Some differences can be observed for longer embedding lengths. Specifically, the SE model is unsuitable for representing the SMA's behaviour after the plateau. In the case of the $1''$ KR specimen, all the SMA models overestimate the debonding force, and the model that better fits the experimental results is the SME. In the $3''$ specimen simulations, the force required to break the SMA is not reached, and debonding occurs.

In Fig. 12, the distribution along the interface of the CZM normal and tangential tractions of both EP and KR $1''$ simulations are illustrated for different instants at different pull-out displacements, with the last one just before complete debonding. On the right, are also represented *Mode I* and *II* contribution during pull-out simulations, calculated from Ref. [59]:

$$\left(\frac{t_n}{t_{n,max}}\right)^2 + \left(\frac{t_t}{t_{t,max}}\right)^2 = 1 \tag{3}$$

where t_n and t_t are the maximum tractions in the simulation substep considered, while $t_{n,max}$ and $t_{t,max}$ are *Mode I* and *Mode II* maximum traction separation (e.g. *Mode I* contribution is evaluated as $(t_n/t_{n,max})^2$). It must be pointed out that the results for KR simulations partially represent the real normal deformation of the thick elastomeric layer due to the missing coupling with the tangential deformation, as observed in Section 3.3.2.

In EP tangential traction graphs, a tension gradient is observed, which develops over a maximum length of 7 mm and advances as delamination progresses. This should be the same critical length observed by Payandeh [35], at which the IFSS becomes independent of L_e. This length is about the same ($1/4''$) as observed in the experimental section at which the stiffness stops to increase, $L_{e,k}$. This can be attributed to the fact that, in specimens with $L_e < L_{e,k}$, the tangential stress is distributed along the entire length and acts on a smaller interface, thus resulting in an overall reduced stiffness. When the length still adhered is less than the length of the gradient, the tension redistributes, and the maximum peak increases due to the simultaneous drastic reduction in normal traction, observable in the modes contribution graph.

Regarding the trend of KR tangential traction, as delamination progresses, distribution along the entire embedding length can be observed with a bilinear trend due to the MT in the embedded wire. The distribution is significantly longer than $1''$, and $L_{e,k}$ is likely longer than the experimental estimation. For both EP and KR, as observed in the experimental results, the tangential stress becomes almost constant with the progression of the delamination and the reduction of the adhered wire length. Detachment happens, as expected, at a length approximately equal to $L_{e,c}$: around 2 and 5 mm for EP and KR, respectively, from last tangential traction curve (in Fig. 12 the green curves at 4.1 mm and 5.2 mm pull-out displacement of EP and KR, respectively). *Mode I* is negligible at this length, observing the energy contribution graph in Fig. 12. Therefore, Eq. (1) pure *Mode II* approximation for $L_e \leq L_{e,c}$ looks reasonable. Moreover, it can be observed that EP *Mode I* value oscillation is noticeable, probably due to large values of the interface stiffness that may cause numerical instability, such as spurious oscillations of the tractions [60]. It is also evident that there is a different crack propagation between EP and KR. In EP, when the MT reach the embedded wire, at around 1.5 mm pull-out displacement (Fig. 12), there is an increment in *Mode I* and *II*. Both contribute to delamination starting in equal measure [30], but the increment of the normal stress is critical and decisive for delamination initiation and propagation (EP cannot

Table 6
Fine-tuned values for the CZM parameters of EP and KR.

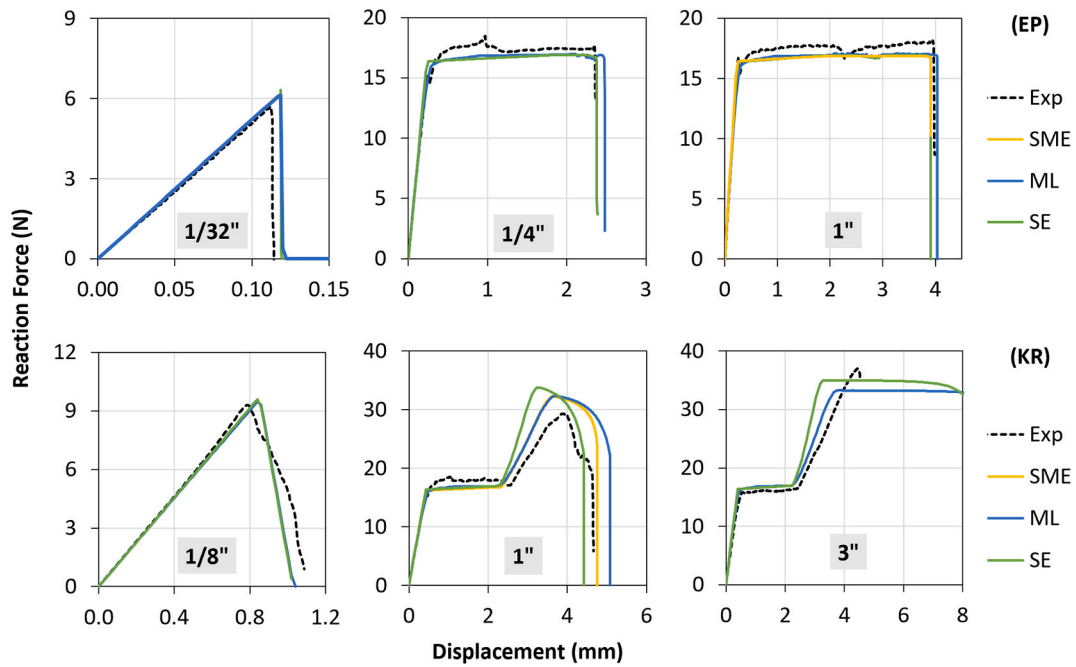|	$t_{n,max}$ (MPa)	δ_n^* (mm)	$\delta_{n,C}$ (mm)	GI (MPa*mm)	$t_{t,max}$ (MPa)	δ_t^* (mm)	$\delta_{t,C}$ (mm)	GII (MPa*mm)
EP	1.9	0.0023	0.0024	0.0023	13.5	0.040	0.042	0.28
KR	2.8	0.15	0.21	0.29	4.8	0.72	1.03	2.48

Fig. 11. Results of CZM validation simulations compared with the experimental result (black dotted curve) for different representative embedding lengths. The first row shows EP results, while the second row shows KR results.
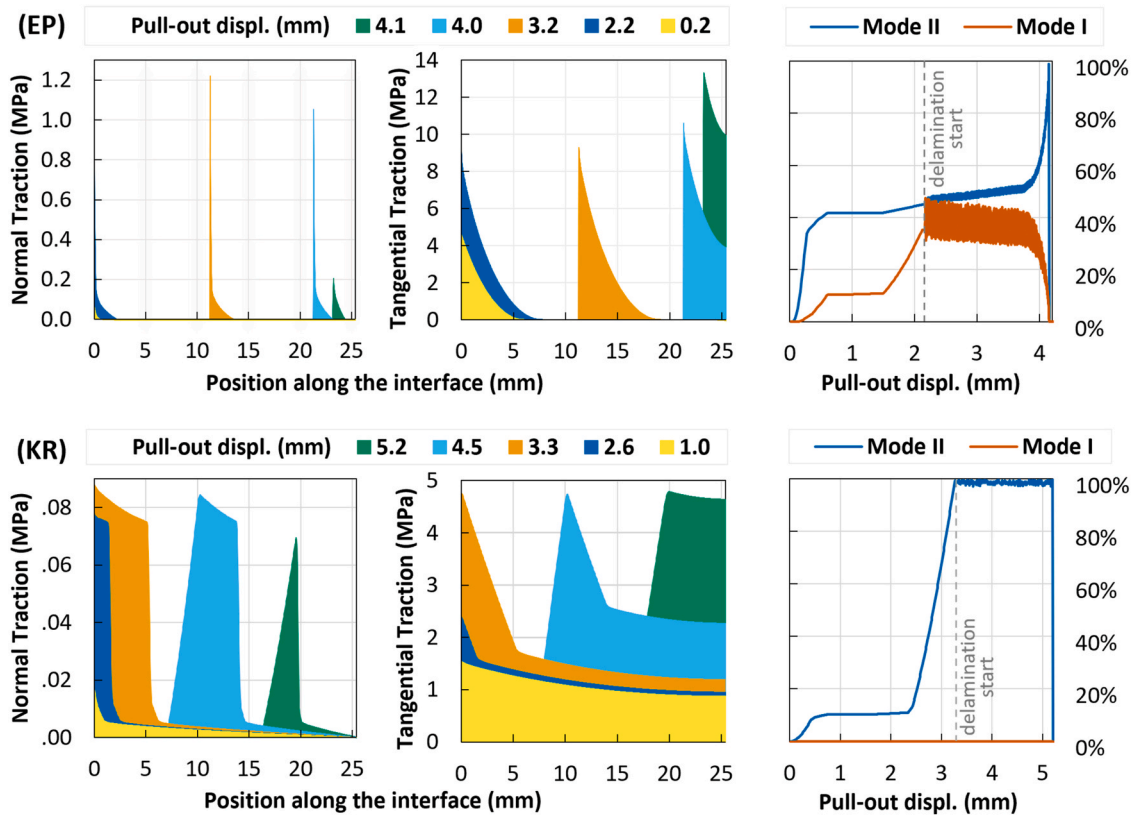

Fig. 12. CZM simulations results for 1″ EP (upper row) and KR (lower raw). Normal and tangential traction along the interface for selected sub-steps of the pull-out displacement are reported. The graph on the right represents *Mode I* (blue line) and *Mode II* (orange line) contributions in percentage, calculate from Eq. (3) during the pull-out simulations.

withstand the high MT-induced radial deformation). Just before complete debonding, an increase of Mode II and a reduction of the *Mode I* contributions is observed. Meanwhile, in KR, the contribution of normal stress is always negligible because the elastomer can deform more than

the epoxy and better follow the SMA profile change in tangential and radial direction during MT.

In conclusion, the numerical analysis shows that using FEM with shared nodes is a valuable method for evaluating RTS and estimating

first-attempt values for CZM models. As anticipated in Ref. [31], RTS were negligible in the KR case. However, the shared nodes EP model resulted in overestimated stress gradients, due to the absence of the CZM interface that correctly models the epoxy interlayer between GFRP and SMA wire. On the other hand, the KR shared nodes model better represent the stress gradient, due to the solid modelling of the elastomeric interlayer.

The implementation of CZM proved to be advantageous in accurately simulating the behaviour of interfaces debonding. Notably, the CZM simulation of the EP interface exhibited a strong correspondence with the experimental data, effectively representing both force and debonding behaviour across all lengths. The only factor not accounted for was the minor increase in force during debonding caused by debris on the wire. In CZM simulations of the KR specimen, lower lengths are accurately approximated. However, it is observed that experimental results are less effective with higher length and deformations. It is believed that the cause of this issue is the inaccurate portrayal of KRAIBON's deformation behaviour by the CZM mono-dimensional element, which struggled with accurately depicting the large deformation that occurred in the thick and compliant KR elastomeric layer, as can be observed in the shared nodes simulations in Fig. 13 (note that the deformation is real and not amplified).

Because of this, normal and tangential tractions are probably underestimated; shared nodes simulation gave for the maximum interfacial shear stress 7 MPa and for the normal stress around 3 MPa, compared to the 4.8 MPa and 0.09 MPa for the CZM one, respectively. Unfortunately, the CZM model fails to consider these factors. Therefore, it is necessary either represent the elastomeric geometry fully in addition to the CZM interface [61] (with high element distortion and convergence problems) or to use a CZM that considers the coupled effect of tangential and radial stress such as the potential-based for mixed-mode cohesive fracture formulation [62,63]. Furthermore, changes in Young's modulus and hardness because of the MT of the SMA may affect the wire's surface characteristics, resulting in a variation of the adhesive behaviours [9,20,36].

4. Proof of concept

To prove the advantage of the elastomeric interface solution, a lamination of a morphing capable SMAHC was designed with FEA, manufactured and tested. SMA wire with shape memory effect (Austenite start temp. $A_s = 90\,°C$) and 0.5 mm diameter were employed. Wire was preloaded with 35 N and locked during curing to avoid recovering of the shape. The stacking sequence was: [CFRP$_{UD}$-$0°_1$/ GFRP-$0°_1$/KRAIBON$_1$/SMA/KRAIBON$_1$/GFRP-$0°_1$].

The SMA wire was turned in the plane of the lamination back and forth 6 times, with a pitch of 5 mm. The final dimensions of the specimen was 100 mm × 300 mm x 2.5 mm. The tests were carried out using a current generator, in which activation, i.e., morphing, occurs due to the wire being heated by the Joule effect. Despite the loss of stress transfer due to the compliance of the elastomeric interface, the designed SMAHC was capable of transmitting enough force for an effective actuation: 100 times repetition displayed 50–60 mm vertical displacement without any visible wire delamination. In Fig. 14 the setup and the sequence of

activation is shown.

5. Conclusions

It is well known that the mechanical behaviour of SMAHCs depends largely on the properties of the fibre/matrix interface. Several methods to improve adhesion have been proven to increase the IFSS, drastically modifying the SMA surface or using complex processing. However, none of the results in the literature could sustain the large deformation in the embedded wire, without debonding and reaching the breaking of the SMA wire.

In this study, the use of KRAIBON® as an elastomeric interface proved to be simple and effective solution to enhance the performance of SMAHCs. Pull-out tests were performed on SMAHC GFRP specimens of different lengths, with or without the KRAIBON® interface. Experimental results showed the ability of KRAIBON® to sustain the large strains that occurs during martensitic transformation, in both the tangential and radial directions, without debonding, leading to SMA wire breakage.

The FEA showed that the elastomeric interface can reduce the residual thermal stresses by orders of magnitude. This reduces the risk of delamination at the interface during the cure cycle. The poposed methodology for the fine tuning of the CZM parameters allow to save time and resources in the material design process. The finite element models were validated on the experimental pull-out tests and revealed the debonding mechanisms; however, highlighting the importance of correctly representing the physics of the highly deformable elastomeric interface. Numerical simulations revealed that the key factor for enhancing SMA adhesion with KRAIBON is to accommodate the high radial contraction that occurs during the martensitic transformations.

The proposed wire embedding solution, by the interleaving an elastomeric interface, open the possibility of fabricating SMA actuated composites with an effective and reliable method for shape morphing applications. The proposed wire embedding solution, which interleaves an elastomeric interface, opens the possibility of fabricating actuated composites for shape-morphing applications using a simple and effective method. Although the elastomeric interlayer has high compliance, which allows stress redistribution and avoids pull-out, it can still drive the load transfer between the SMA wire and the laminate, demonstrating impressive morphing capabilities over several cycles.

Declaration of generative AI and AI-assisted technologies in the Writing

The authors utilised the Grammarly generative AI tool to enhance the readability and language of this work. Subsequent to utilising this tool, the authors thoroughly reviewed and edited the content as required and hereby assume full responsibility for the publication's contents.

CRediT authorship contribution statement

Gregorio Pisaneschi: Writing – review & editing, Writing – original draft, Validation, Supervision, Resources, Project administration, Methodology, Investigation, Formal analysis, Data curation,
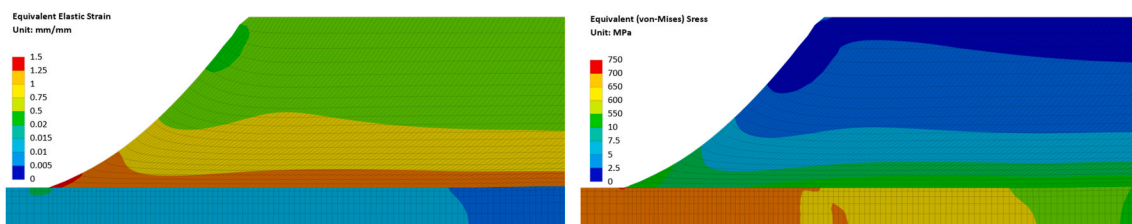

Fig. 13. KR 1″ shared nodes simulation results while MT start propagate in the embedded wire. On the left is the equivalent strain; on the right is the equivalent (von-Mises) stress. Additional results are reported in supplementary Section 3.
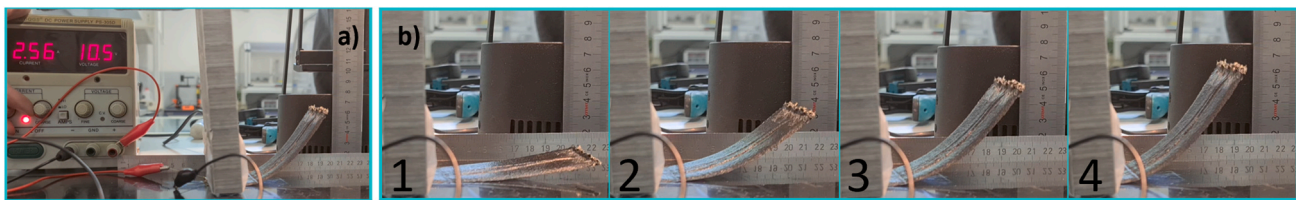
Fig. 14. a) experimental setup with the maximum voltage and current. b) 1–4 SMAHC sequence of the activation.

Appendix A. Supplementary data

Supplementary data to this article can be found online at https://doi.org/10.1016/j.compositesb.2024.111785.

References

[1] Lagoudas DC. Shape memory alloys. Boston, MA: Springer US 2008;1(8).
[2] Scalet G, Conti M, Auricchio F. Computational analysis of advanced shape-memory alloy devices through a robust modeling framework. Shape Mem. Superelasticity Jun. 2017;3(2):109–23.
[3] Mohd Jani J, Leary M, Subic A, Gibson MA. A review of shape memory alloy research, applications and opportunities. Mater Des Apr. 2014;56:1078–113.
[4] Ashby MF, Bréchet YJM. Designing hybrid materials. Acta Mater Nov. 2003;51(19):5801–21.
[5] Lester BT, Baxevanis T, Chemisky Y, Lagoudas DC. Review and perspectives: shape memory alloy composite systems. Acta Mech Dec. 2015;226(12):3907–60.
[6] Han M-W, et al. Woven type smart soft composite for soft morphing car spoiler. Composites Part B Feb. 2016;86:285–98.
[7] Kaiser M, Kunzler M, Gurka M. Experimentally characterization and theoretical modeling of the electro-thermomechanical coupling of unimorph Shape Memory Active Hybrid composites. Compos Sci Technol Sep. 2023;242(March):110186.
[8] Berman JB, White SR. Theoretical modelling of residual and transformational stresses in SMA composites. Smart Mater Struct Dec. 1996;5(6):731–43.
[9] Bettini P, Riva M, Sala G, Di Landro L, Airoldi A, Cucco J. Carbon fiber reinforced smart laminates with embedded SMA actuators—Part I: embedding techniques and interface analysis. J Mater Eng Perform Aug. 2009;18(5–6):664–71.
[10] Xu Y, et al. A new method for fabricating SMA smart polymer matrix composites. Adv Eng Mater 2002;4(9):683–6.
[11] Kirkby EL, O'Keane J, de Oliveira R, Michaud VJ, Månson J-AE. Tailored processing of epoxy with embedded shape memory alloy wires. Smart Mater Struct Sep. 2009;18(9):095043.
[12] Baz A, Ro J. Thermo-dynamic characteristics of composite beams. Mech Eng 1992;2:527–42.
[13] Kluge A, Henneberg J, Nocke A, Cherif C. Methods for adhesion/friction reduction of novel wire-shaped actuators, based on shape memory alloys, for use in adaptive fiber-reinforced plastic composites. J Ind Text Mar. 2015;44(5):757–68.
[14] Paine J, Jones W, Rogers C. Nitinol actuator to host composite interfacial adhesion in adaptive hybrid composites. In: 33rd structures, structural dynamics and materials conference; 1992.
[15] Jonnalagadda K, Kline GE, Sottos NR. Local displacements and load transfer in shape memory alloy composites. Exp Mech Mar. 1997;37(1):78–86.
[16] Furst SJ, Bumgarner D, Seelecke S. "Quantification of the effectiveness of various conductive and non-conductive epoxies as an attachment method for small SMA wires," in *volume 2: multifunctional materials; enabling Technologies and integrated system design*. Structural health monitoring/NDE; bio-inspired smart materials and structures. 2009. p. 409–18.
[17] Rey T, et al. Mechanical characterization and comparison of different NiTi/silicone rubber interfaces. Int J Adhesion Adhes Jan. 2014;48:67–74.
[18] Jang BK, Kishi T. Adhesive strength between TiNi fibers embedded in CFRP composites. Mater Lett May 2005;59(11):1338–41.
[19] Smith NA, Antoun GG, Ellis AB, Crone WC. Improved adhesion between nickel–titanium shape memory alloy and a polymer matrix via silane coupling agents. Compos. Part A Appl Sci Manuf Nov. 2004;35(11):1307–12.
[20] Rossi S, Deflorian F, Pegoretti A, D'Orazio D, Gialanella S. Chemical and mechanical treatments to improve the surface properties of shape memory NiTi wires. Surf Coating Technol Feb. 2008;202(10):2214–22.
[21] Neuking K, Abu-Zarifa A, Eggeler G. Surface engineering of shape memory alloy/polymer-composites: improvement of the adhesion between polymers and pseudoelastic shape memory alloys. Mater Sci Eng May 2008;481–482(1–2 C):606–11.
[22] Hamming L, Fan X, Messersmith P, Brinson L. Mimicking mussel adhesion to improve interfacial properties in composites. Compos Sci Technol Jul. 2008;68(9):2042–8.
[23] Lau K, Tam W, Meng X, Zhou L. Morphological study on twisted NiTi wires for smart composite systems. Mater Lett Dec. 2002;57(2):364–8.
[24] Yuan G, Bai Y, Jia Z, Hui D, Lau K. Enhancement of interfacial bonding strength of SMA smart composites by using mechanical indented method. Composites Part B Dec. 2016;106:99–106.
[25] Choi E, Kim D, Lee J-H, Ryu G-S. Monotonic and hysteretic pullout behavior of superelastic SMA fibers with different anchorages. Composites Part B Jan. 2017;108:232–42.
[26] Kim DJ, Kim HA, Chung Y-S, Choi E. Pullout resistance of straight NiTi shape memory alloy fibers in cement mortar after cold drawing and heat treatment. Composites Part B Dec. 2014;67:588–94.
[27] Lau K-T, Chan AW-L, Shi S-Q, Zhou L-M. Debond induced by strain recovery of an embedded NiTi wire at a NiTi/epoxy interface: micro-scale observation. Mater Des May 2002;23(3):265–70.
[28] Poon C, Lau K, Zhou L. Design of pull-out stresses for prestrained SMA wire/polymer hybrid composites. Composites Part B Jan. 2005;36(1):25–31.
[29] Eyer P, Dittus J, Trauth A, Coutandin S, Fleischer J, Weidenmann KA. Improvement of the adhesion in functional NiTi wire/polymer composites made by additive manufacturing. Compos Struct Nov. 2021;275(August):114455.
[30] Antico FC, Zavattieri PD, L Jr GH. Adhesion of nickel-titanium shape memory alloy wires to polymeric materials: theory and experiment. In: Supplemental proceedings, vol. 2. Hoboken, NJ, USA: Wiley; 2012. p. 563–76. June.
[31] Povolo M, Brugo TM, Zucchelli A. Numerical and experimental investigation of aluminum/CFRP hybrid tubes with rubber-like interlayer. Appl Compos Mater Jun. 2020;27(3):269–83.
[32] Pisaneschi G, Brugo TM, Cosseddu P, Scalet G, Zucchelli A. Experimental and numerical investigation of shape memory alloy hybrid composites with elastomeric interface. In: ICCM international conferences on composite materials; 2023.
[33] Kelly A, Tyson WR. Tensile properties of fibre-reinforced metals: copper/tungsten and copper/molybdenum. J Mech Phys Solid Dec. 1965;13(6):329–50.
[34] Volkersen O. Rivet strength distribution in tensile-stressed rivet joints with constant cross-section. Luftfahrforschung 1938;15(1):41–7.
[35] Payandeh Y, Meraghni F, Patoor E, Eberhardt A. Debonding initiation in a NiTi shape memory wire–epoxy matrix composite. Influence of martensitic transformation. Mater Des Mar. 2010;31(3):1077–84.
[36] Barrie F, Futch DB, Hsu DHD, Manuel MV. Effect of phase on debond strength in shape memory alloy reinforced composites. Mater Des May 2014;57:98–102.
[37] Sadrnezhaad SK, Nemati NH, Bagheri R. Improved adhesion of NiTi wire to silicone matrix for smart composite medical applications. Mater Des Oct. 2009;30(9):3667–72.
[38] Pattar N, Patil SF. Review on fabrication and mechanical characterization of shape memory alloy hybrid composites. Adv Compos Hybrid Mater 2019;2(4):571–85.
[39] Zhou LM, Kim JK, Mai YW. On the single fibre pull-out problem: effect of loading method. Compos Sci Technol 1992;45(2):153–60.
[40] Yue CY, Looi HC, Quek MY. Assessment of fibre-matrix adhesion and interfacial properties using the pull-out test. Int J Adhesion Adhes Apr. 1995;15(2):73–80.

[41] Churchill CB, Shaw JA, Iadicola MA. Tips and tricks for characterizing shape memory alloy wire: part 4 - thermo-mechanical coupling. Exp Tech Mar. 2010;34 (2):63–80.

[42] Pagliaro A, Panciroli R. On the use of ductile tabs as a viable strategy to test SMA and other high-strength fine wires. Mater Des Jul. 2021;205:109727.

[43] Otsuka K, Ren X. Physical metallurgy of Ti-Ni-based shape memory alloys. Prog Mater Sci 2005;50(5):511–678.

[44] Anderson TL. Fracture mechanics. CRC Press; 2017.

[45] Dawood M, El-Tahan MW, Zheng B. Bond behavior of superelastic shape memory alloys to carbon fiber reinforced polymer composites. Composites Part B Aug. 2015;77:238–47.

[46] Chua PS, Piggott MR. The glass fibre-polymer interface: II—work of fracture and shear stresses. Compos Sci Technol Jan. 1985;22(2):107–19.

[47] HexPly® Prepreg." [Online]. Available: www.hexcel.com/user_area/content_med ia/raw/Prepreg_Technology.pdf.

[48] Auricchio F, Taylor RL, Lubliner J. Shape-memory alloys: macromodelling and numerical simulations of the superelastic behavior. Comput Methods Appl Mech Eng Jul. 1997;146(3–4):281–312.

[49] Souza AC, Mamiya EN, Zouain N. Three-dimensional model for solids undergoing stress-induced phase transformations. Eur J Mech Solid Sep. 1998;17(5):789–806.

[50] Auricchio F, Petrini L. A three-dimensional model describing stress-temperature induced solid phase transformations: thermomechanical coupling and hybrid composite applications. Int J Numer Methods Eng Oct. 2004;61(5):716–37.

[51] Auricchio F, Coda A, Reali A, Urbano M. SMA numerical modeling versus experimental results: parameter identification and model prediction capabilities. J Mater Eng Perform Aug. 2009;18(5–6):649–54.

[52] Hahn HT. Residual stresses in polymer matrix composite laminates. J Compos Mater Oct. 1976;10(4):266–78.

[53] Kelly P, Akelah A, Qutubuddin S, Moet A. Reduction of residual stress in montmorillonite/epoxy compounds. J Mater Sci May 1994;29(9):2274–80.

[54] Lei H, Wang Z, Zhou B, Tong L, Wang X. Simulation and analysis of shape memory alloy fiber reinforced composite based on cohesive zone model. Mater Des Sep. 2012;40(September 2012):138–47.

[55] Cox HL. The elasticity and strength of paper and other fibrous materials. Br J Appl Phys Mar. 1952;3(3):72–9.

[56] Alfano G, Crisfield MA. Finite element interface models for the delamination analysis of laminated composites: mechanical and computational issues. Int J Numer Methods Eng Mar. 2001;50(7):1701–36.

[57] Lindgaard E, Bak BLV, Glud JA, Sjølund J, Christensen ET. A user programmed cohesive zone finite element for ANSYS Mechanical. Eng Fract Mech Jul. 2017;180: 229–39.

[58] Leuschner M, Fritzen F, van Dommelen JAW, Hoefnagels JPM. Potential-based constitutive models for cohesive interfaces: theory, implementation and examples. Composites Part B Jan. 2015;68:38–50.

[59] Brewer JC, Lagace PA. Quadratic stress criterion for initiation of delamination. J Compos Mater Dec. 1988;22(12):1141–55.

[60] Turon A, Dávila CG, Camanho PP, Costa J. An engineering solution for mesh size effects in the simulation of delamination using cohesive zone models. Eng Fract Mech 2007;74(10):1665–82.

[61] Meng Q, Chang M. Interfacial crack propagation between a rigid fiber and a hyperelastic elastomer: experiments and modeling. Int J Solid Struct 2020; 188–189:141–54.

[62] Park K, Paulino GH, Roesler JR. A unified potential-based cohesive model of mixed-mode fracture. J Mech Phys Solid Jun. 2009;57(6):891–908.

[63] Park K, Paulino GH. Computational implementation of the PPR potential-based cohesive model in ABAQUS: educational perspective. Eng Fract Mech Oct. 2012; 93:239–62.